

CMOS characterization and calculation of atmospheric extinction coefficient

Using Growth India Telescope, Hanle

Anvit Khade, Arya Joshi, Ronit, Gokul Ramanan



CMOS characterization and calculation of atmospheric extinction coefficient

Using Growth India Telescope, Hanle

PH556 Astrophysics Course Project

Author(s): Anvit Khade, Arya Joshi, Ronit, Gokul Ramanan
Student ID: 23b1828, 23B1853, 23B1837, 23B1854
Supervisor: Varun Bhalerao
Facilitator: Aditya Saikia
Project duration: Oct 2025 – Nov 2025

Cover image: Indian Institute of Astrophysics - website
Template style: Thesis style by Richelle F. van Capelleveen
Template licence: Licenced under CC BY-NC-SA 4.0



STAR Lab - Indian Institute of Technology Bombay, Powai - 400076

Abstract

This work presents a comprehensive characterization of the CMOS detector system and an analysis of atmospheric extinction using observations from the 70cm Growth India Telescope (GIT,) Hanle. To evaluate detector performance, calibration data consisting of bias, dark, and flat field frames were acquired. The CCD gain was determined using both the mean–variance (photon transfer) method and the Monitors method. Atmospheric extinction was quantified through multiple observations with varying airmass values of the open cluster NGC 1039 in the SDSS ugriz filter set. Instrumental magnitudes obtained through aperture photometry were modeled using Bouguer’s law to estimate extinction coefficients. The extinction values show a wavelength-dependent trend consistent with previous studies of Hanle skies such as Stalin et al. (2008). Moreover, a non-linear trend in airmass was noted at high zenith angles, highlighting limitations of the simple sec Z approximation.

Contents

Abstract	iii
1 Introduction	1
1.1 Overview of the Growth India Telescope	2
1.2 Background and Objectives	2
2 Theory and Principles	3
2.1 CMOS Imaging Principles	3
2.2 Key Performance Parameters in CMOS	5
2.3 Atmospheric Extinction Fundamentals	6
2.3.1 Air Mass	6
2.3.2 Effect of extinction on magnitude	7
3 CMOS Characterization	8
3.1 Data Acquisition	8
3.2 Preprocessing of Flat Frames	8
3.3 Gain Determination Methods	8
3.4 Results	9
4 Atmospheric Extinction	11
4.1 Target selection	11
4.2 Data acquisition and pipeline	12
4.3 Results	13
5 Discussion	16
6 Conclusion	18
Bibliography	19

1 . Introduction

Accurate photometric measurements are essential for understanding astrophysical phenomena, yet their reliability depends strongly on two factors: (instrumental) detector performance and (environmental) atmospheric transparency. Even with modern instruments, uncertainties in detector response, such as gain, read noise, and dark current, can introduce significant errors in measured fluxes. Therefore, proper detector characterization is critical to ensure that observational data reflect a true signal rather than instrumental effects.

In addition, light from astronomical sources is attenuated as it passes through Earth's atmosphere due to scattering and absorption. This atmospheric extinction varies with wavelength and observing conditions, making it necessary to measure extinction coefficients to accurately correct observed magnitudes. Without such corrections, comparisons across different epochs, filters, or observations are unreliable to a certain extent.



Figure 1.1: Observatorios de Canarias by de Astrofísica de Canarias (IAC)

1.1 Overview of the Growth India Telescope

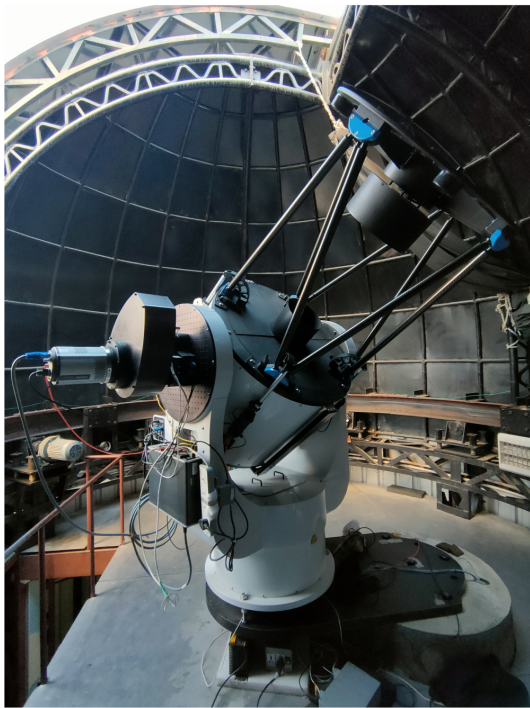


Figure 1.2: GROWTH-India Telescope inside the enclosure. The Andor camera is shown mounted on the telescope. Kumar et al. (2022)

The Growth India Telescope (GIT) is located at the Indian Astronomical Observatory in Hanle, Ladakh, at an altitude of about 4500 meters, making it one of the highest and best astronomical sites globally. The high elevation results in thin, stable air, ideal for accurate atmospheric extinction measurements.

GIT is a 70 cm aperture, f/6.5 Corrected Dall-Kirkham (CDK700) optical telescope mounted on an Altitude-Azimuth mount, offering precise and efficient tracking. The telescope's design provides a wide field of view (0.7° squared) suited for time-domain astronomy and transient event monitoring.

Note For detector characterization, the telescope uses an SBIG STC-428 OEM CMOS camera featuring a 1944×1472 -pixel sensor with $7.4 \mu\text{m}$ pixels.

The CMOS sensor is thermoelectrically cooled to suppress dark current and improve low-noise performance. This is the secondary camera of GIT, the adjacent image shows the primary camera being used.

1.2 Background and Objectives

Complementary Metal–Oxide–Semiconductor (CMOS) detectors have become increasingly important in astronomical imaging due to their low power consumption, rapid readout, and steadily improving noise performance. Their characterization is essential to fully understand and correct for instrumental effects such as gain variations, read noise, and dark current. Alongside instrumental calibration, Earth's atmosphere significantly influences observations through extinction caused by scattering and absorption processes. Accurate determination of atmospheric extinction coefficients is therefore crucial for correcting raw photometric data to obtain true astrophysical measurements. This project aims to comprehensively characterize the CMOS detector used with the Growth India Telescope and quantify the atmospheric extinction affecting its observations. The objectives include determining aforementioned CMOS performance parameters as well as calculating atmospheric extinction coefficients using observed data.

2 . Theory and Principles

2.1 CMOS Imaging Principles

Two different underlying technologies are used in today's astronomical cameras: charge coupled devices (CCD) and complementary metal oxide semiconductors (CMOS). CCD technology is older, and most semiconductor manufacturers have switched to the fabrication of CMOS sensors exclusively. Both technologies have been used very successfully for photometry; neither technology has inherently superior photometric performance. However, the supporting circuitry is quite different between CCD and CMOS cameras, and these differences result in different camera characteristics

In CMOS, during an exposure, photons generate electrons that accumulate in the pixel's potential well. After exposure, the reset transistor clears the pixel, and then the accumulated charge is converted to voltage through the local amplifier. The pixels are read row by row using active pixel circuitry, and the signals are digitized through column-parallel readout chains that lead to the ADC.

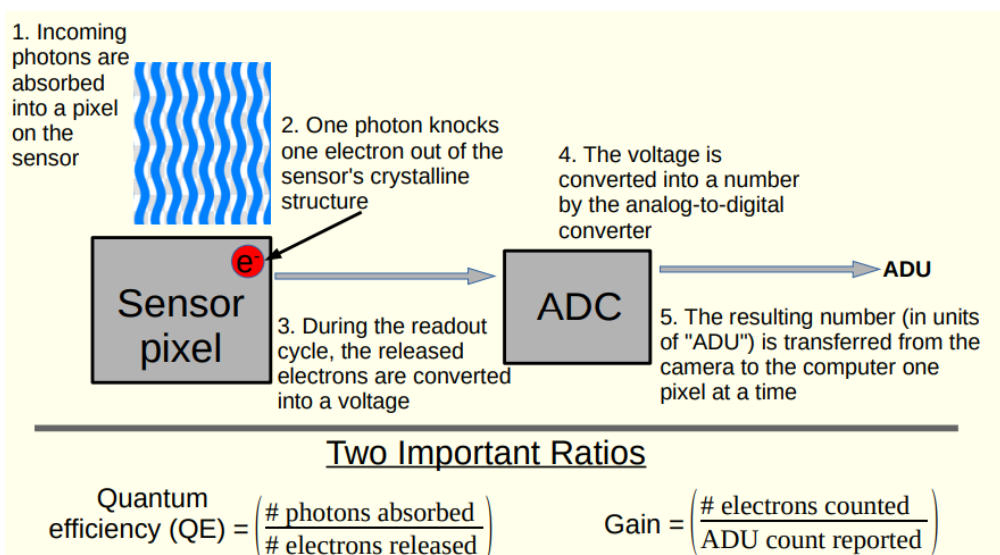


Figure 2.1: Working of a CMOS sensor aav (2022)

Accurate characterization of a CMOS detector relies on acquiring three standard calibration frame types: **bias**, **dark**, and **flat-field** frames.

- **Bias frames** (zero exposure):

Bias frames are taken with the shutter closed and zero exposure time. They record the electronic offset introduced during readout, ensuring that no pixel has a negative value after digitization. Bias frames contain the bias level, fixed-pattern bias structure, and read noise.

- **Dark frames** (finite exposure, shutter closed):

Dark frames measure thermally generated electrons that accumulate during an exposure. They contain contributions from dark current. A master dark is produced by averaging multiple dark frames, and is used to correct science images for thermal signal.

- **Flat-field frames** (uniform illumination):

Flat fields are obtained under spatially uniform illumination, such as twilight sky or a dome screen. They measure pixel-to-pixel sensitivity variations, optical vignetting, and dust shadows on the optical path.

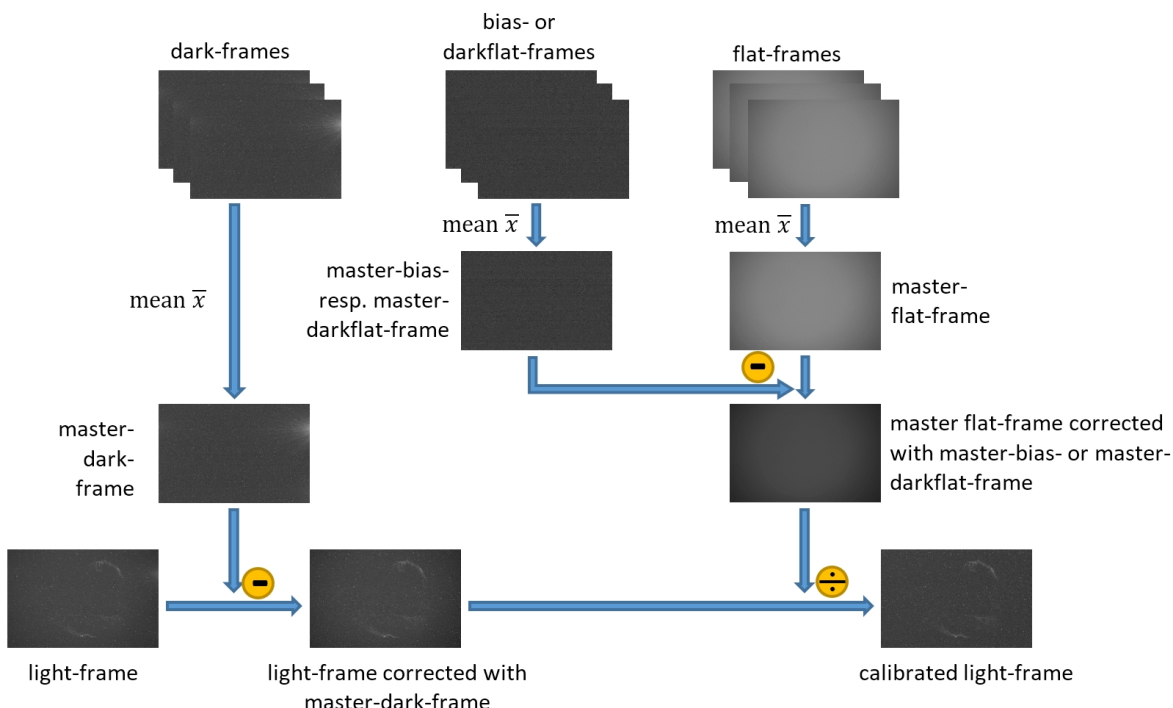


Figure 2.2: Schematic illustration of the use of the calibration images in the creation of a corrected light frame, using the Cirrus Nebula as an example [\(2022\)](#)

2.2 Key Performance Parameters in CMOS

Gain

When photons strike a pixel's photodiode, they produce electrons proportional to the local intensity. These electrons are converted to a voltage inside the pixel or column amplifier and then digitized by an ADC. The **gain** represents the conversion factor between the number of electrons and the digital count (ADU):

$$G \equiv \frac{\text{electrons}}{\text{ADU}} \quad (2.1)$$

Gain determines how efficiently the captured charge is mapped into digital values and is necessary for converting image data into physical units. It is typically measured using photon-transfer methods such as the mean-variance technique or monitor's method, ref. chapter 6.

Read Noise

Read noise represents the uncertainty added during the readout and digitization process. In CMOS since each pixel or column has its own amplifier, read noise can vary across the detector. It can be measured using pairs of bias images:

$$\text{RN} = G \times \frac{\sigma_{\text{diff}}}{\sqrt{2}} \quad (2.2)$$

$$\Delta(\text{RN}) = \frac{G \sigma_{\text{diff}}}{\sqrt{2}} \sqrt{\left(\frac{\Delta G}{G}\right)^2 + \left(\frac{\Delta \sigma_{\text{diff}}}{\sigma_{\text{diff}}}\right)^2} \quad (2.3)$$

where σ_{diff} is the standard deviation of the difference between two bias frames. Modern scientific CMOS sensors have achieved read noise enabling high speed, low light imaging applications.

Dark Current

Dark current arises from thermally generated electrons within the pixel even when no light is present. It increases exponentially with temperature and contributes to background noise. Because readout electronics are integrated into each pixel, thermally active components can increase the dark current relative to CCDs. Therefore, cooling is essential. The dark current is typically characterized by acquiring dark frames at increasing exposure times and measuring the mean signal within a region of interest. Dark current rate is determined from the slope signal vs. exposure time:

$$I_{\text{dark}} = \frac{\Delta S}{\Delta t} \quad (\text{e}^- / \text{pix} / \text{s}) \quad (2.4)$$

$$\delta(I_{\text{dark}}) = \text{Dark Current} \times \sqrt{\left(\frac{\delta G}{G}\right)^2 + \left(\frac{\delta S}{S}\right)^2} \quad (2.5)$$

2.3 Atmospheric Extinction Fundamentals

Light arriving from astronomical sources is partially attenuated as it passes through Earth's atmosphere. This attenuation, known as **atmospheric extinction**, results from absorption and scattering by atmospheric constituents such as molecules, aerosols, and dust. Understanding extinction is crucial for accurately calibrating ground-based photometric measurements.

2.3.1 Air Mass

The amount of atmosphere traversed by incoming starlight is quantified by the **air mass**, denoted X . It is defined relative to the zenith direction, where the path length through the atmosphere is minimal. To first order, assuming a plane-parallel atmosphere, the air mass is approximated as

$$X \approx \sec Z \quad (2.6)$$

where Z is the **zenith angle**, defined as the angle between the incoming light ray and the zenith.

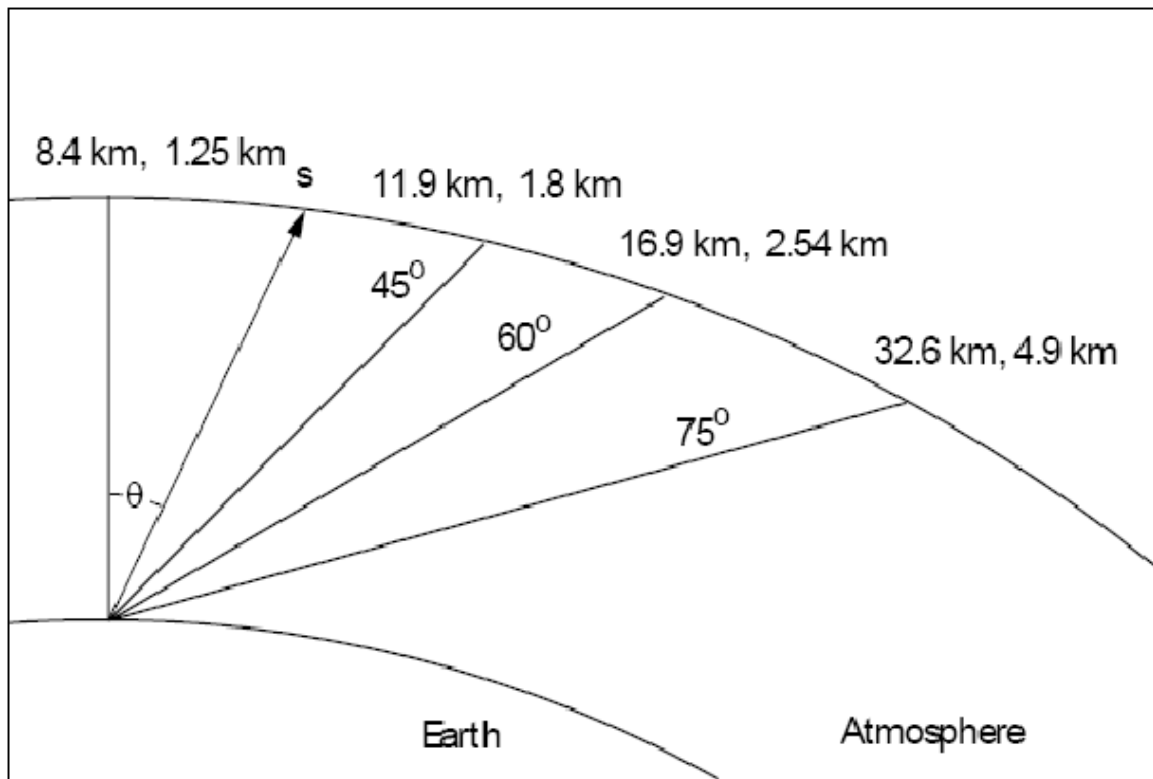


Figure 2.3: Optical length for different paths in the atmosphere Undege (2009)

The above relation is accurate for small to moderate zenith angles ($Z \lesssim 45^\circ$), where atmospheric curvature is negligible. At large zenith angles, $\sec Z$ diverges as $Z \rightarrow 90^\circ$ also earth's curvature and atmospheric refraction become significant. For such cases more accurate empirical expressions are used (e.g. Hardie or Kasten–Young models.)

2.3.2 Effect of extinction on magnitude

Atmospheric extinction refers to the attenuation of starlight as it passes through Earth's atmosphere, caused primarily by scattering and absorption by molecules and aerosols. Although modern differential photometry (such as that used for planetary transit measurements) has achieved millimagnitude precision, linking observations across wide-field sky surveys has not yet reached this level. Pedersen et al. (2025) Differential photometry benefits from simultaneous measurements through the same atmospheric column, but observations separated in time or sky position encounter variable atmospheric transmission. This difference indicates that atmospheric attenuation remains one of the dominant limiting factors for achieving uniform, high precision photometry.

More formally, the detected photon flux Φ from a celestial source may be written Stubbs et al. (2007) as

$$\Phi = \int SPS(\lambda) T_{EG}(\lambda) T_{Gal}(\lambda) T_{atmos}(az, a/t, t, \lambda) T_{inst}(\lambda, t) d\lambda, \quad (2.7)$$

where $SPS(\lambda)$ is the intrinsic source photon spectrum, $T_{EG}(\lambda)$ is transmission due to extragalactic extinction, $T_{Gal}(\lambda)$ is Galactic extinction along the line of sight, $T_{atmos}(az, a/t, t, \lambda)$ denotes atmospheric transmission (explicitly dependent on azimuth, altitude, time, and wavelength), and $T_{inst}(\lambda, t)$ is the instrumental throughput, including detector quantum efficiency. Our primary concern is with T_{atmos} . Under nominal "photometric" conditions, this term is often approximated as depending only on the airmass X .

As starlight traverses the atmosphere, molecular (Rayleigh) scattering, aerosol (Mie) scattering, and absorption, most notably by ozone, reduce the observed flux, increasing the apparent magnitude. The relationship between observed magnitude m' , the outside-atmosphere magnitude m_0 , and airmass X is given by Bouguer's law:

$$m' = m_0 + KX, \quad (2.8)$$

where K is the extinction coefficient, typically expressed in magnitudes per unit airmass. Because extinction varies with wavelength, atmospheric conditions (humidity, aerosol content, dust), and time, K must be measured regularly for high-quality photometry. Although magnitude often varies approximately linearly with X at moderate zenith angles, deviations appear at large airmass due to refraction and curvature effects. We would be using the Bourguer's expression with secZ airmass model to fit our data in chp. 6

3. CMOS Characterization

3.1 Data Acquisition

The CMOS detector was characterized using a standard set of calibration frames. A total of five bias frames (exposure time $\sim 10^{-3}$ s) were acquired to measure the electronic offset. Forty dark frames were taken with the shutter closed at various exposure times to characterize thermally generated dark current. Additionally, five flat-field frames with uniform illumination in the U band filter (5 s exposure) were obtained to correct for pixel-to-pixel sensitivity variations and large-scale illumination gradients.

3.2 Preprocessing of Flat Frames

Prior to analysis, flat-field images were preprocessed to ensure uniformity. A Region of Interest (ROI) was selected by excluding outer vignetted regions of the field to minimize brightness gradients caused by optical vignetting. Within the ROI, a 3σ -clipping algorithm was applied to identify and reject anomalous pixels (e.g. hot or cold pixels) that would otherwise bias the gain and sensitivity estimation.

3.3 Gain Determination Methods

The detector gain was determined using two approaches: the *mean–variance (photon transfer)* method, and the *Monitors* method. Riley et al. (2016)

Mean–Variance (Photon Transfer) Method

The mean–variance method is a widely used technique for estimating detector gain, based on the statistical properties of uniformly illuminated flat-field images. Under Poisson statistics, the variance of the signal increases proportionally with its mean. For sufficiently high signal levels where photon noise dominates, the variance σ^2 in ADU is related to the mean signal μ by

$$\sigma_{\text{ADU}}^2 = \frac{\mu e^-}{G} + \sigma_{\text{read,ADU}}^2 \quad (3.1)$$

or equivalently in ADU-space,

$$\sigma_{\text{ADU}}^2 = \frac{\mu_{\text{ADU}}}{G} + \sigma_{\text{read,ADU}}^2. \quad (3.2)$$

Thus, a plot of variance versus mean should yield a linear relationship, where the slope is the inverse of the detector gain:

$$G = \frac{1}{\text{slope}}. \quad (3.3)$$

Only the linear portion of the graph, well below saturation, is used for fitting.

Monitors Method

The Monitors method provides a more efficient alternative that requires fewer frames. Only two flat frames and two bias frames

$$G = \frac{\text{mean}(flat_1) + \text{mean}(flat_2) - \text{mean}(bias_1) - \text{mean}(bias_2)}{\sigma_{D_{\text{flat}}}^2 - \sigma_{D_{\text{bias}}}^2}. \quad (3.4)$$

3.4 Results

Results of mean-variance

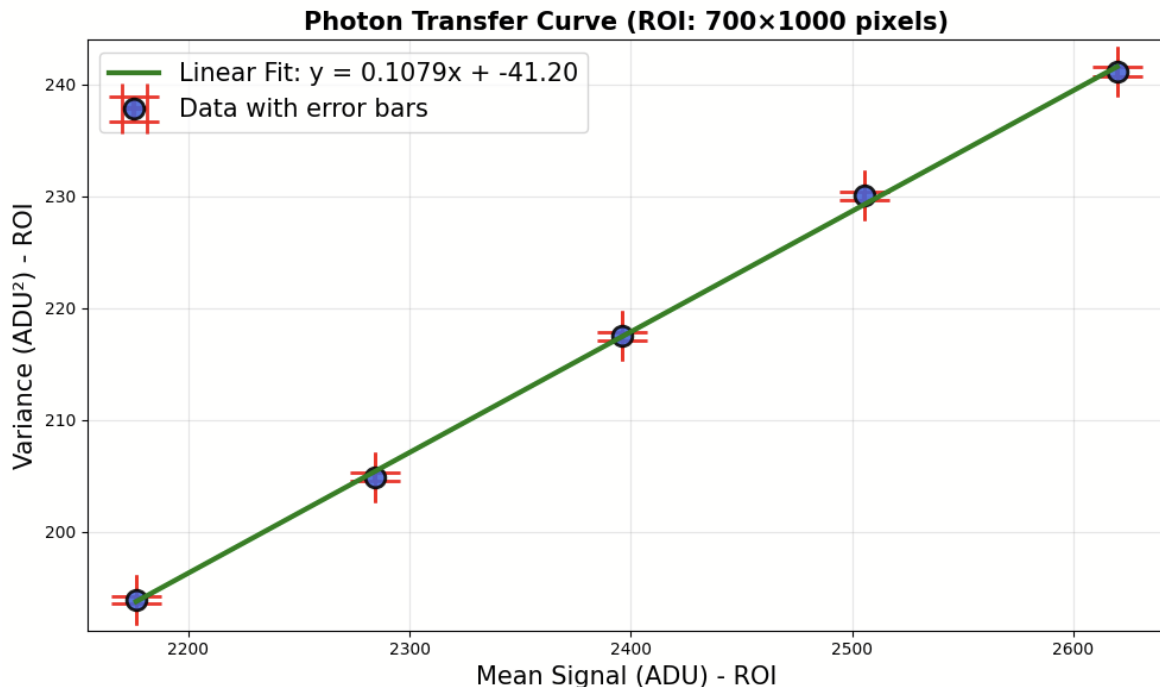


Figure 3.1: Best fit line obtained for Mean-Variance method

Gain = $9.26 \pm 0.14 \text{ e}^-/\text{ADU}$

Read Noise = $6.32 \pm 0.10 \text{ e}^- \text{ RMS}$
--

Results of Monitors Method

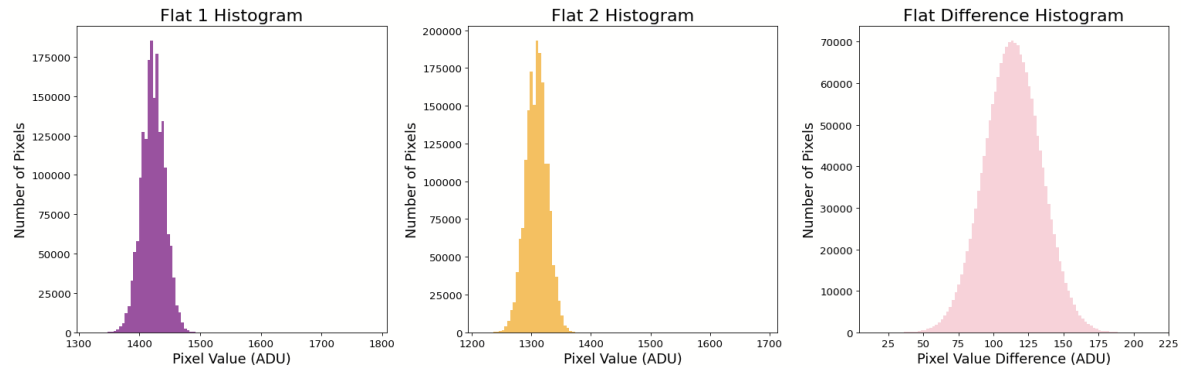


Figure 3.2: Histograms of flat1, flat2 and flat1 - flat2 for visualization

$$\text{Gain} = 9.94 \pm 0.06 \text{ e}^-/\text{ADU}$$

$$\text{Read Noise} = 6.78 \pm 0.04 \text{ e}^- \text{ RMS}$$

Dark current fit

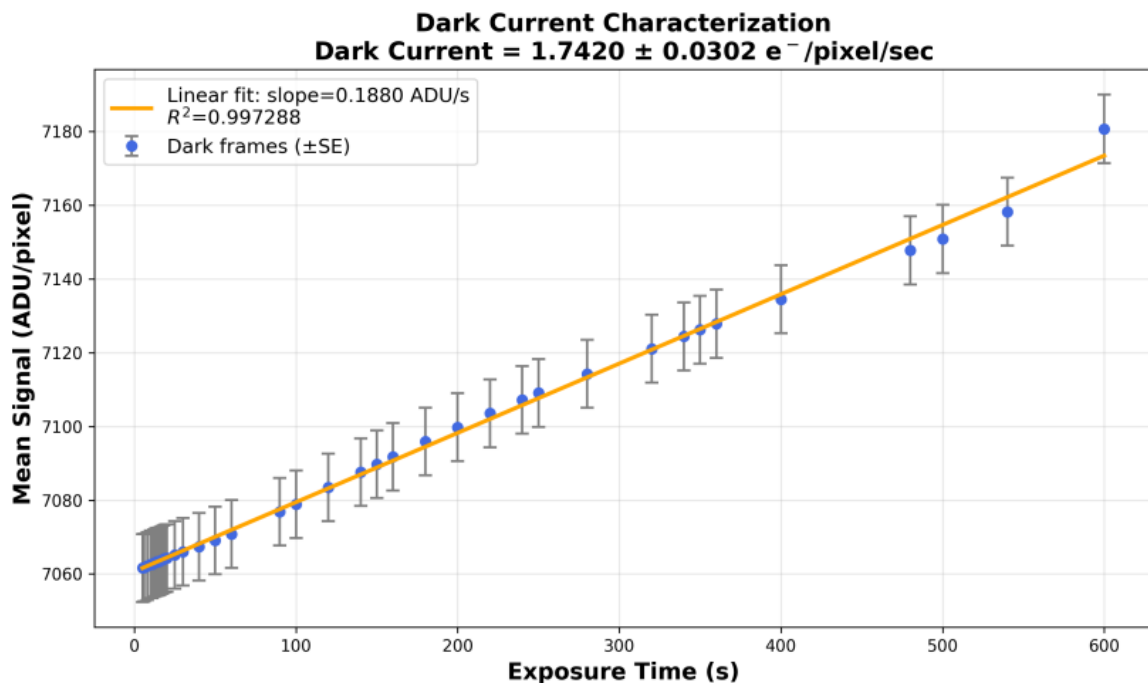


Figure 3.3: Best fit line of mean ADU vs exposure time for 40 dark frames

$$\text{Dark Current} = 1.74 \pm 0.03 \text{ e}^-/\text{pixel/sec}$$

4 . Atmospheric Extinction

4.1 Target selection

The field selected for atmospheric extinction measurement is the dense star cluster **NGC 1039** (a spiral cluster), located at RA $02^{\text{h}}43^{\text{m}}46.8^{\text{s}}$, Dec $+42^{\circ}52'25.6''$. Dense star fields enable simultaneous photometry of many stars, allowing statistical averaging that reduces the influence of individual stellar variability. The target culminates high in the sky, providing access to a wide range of altitudes. (refer 4.4) Observations were carried out during moonless nights with clear sky conditions. Eight images (for each UGRIZ filters) were taken over altitudes ranging from approximately 30° to 76° to sample different atmospheric airmasses.

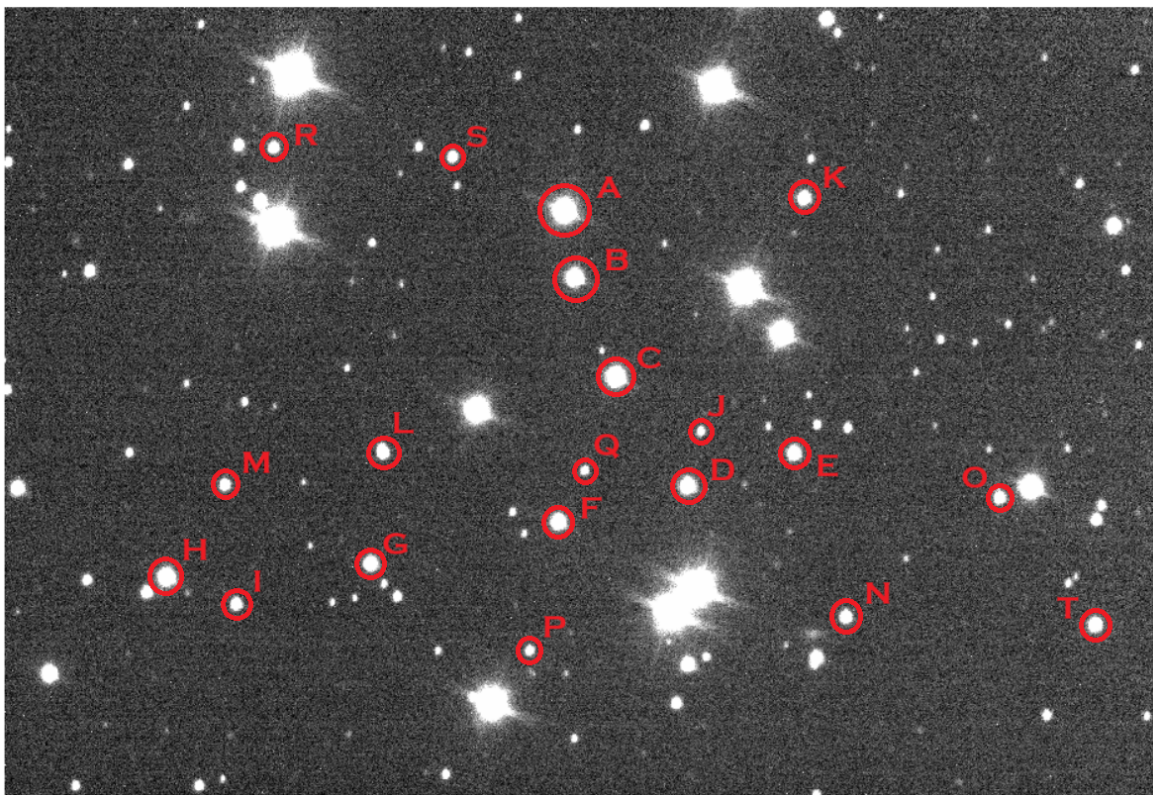


Figure 4.1: NGC1039 Spiral Cluster in G-Band with GIT. Labeled are the chosen 20 stars (A - T) for photometry

4.2 Data acquisition and pipeline

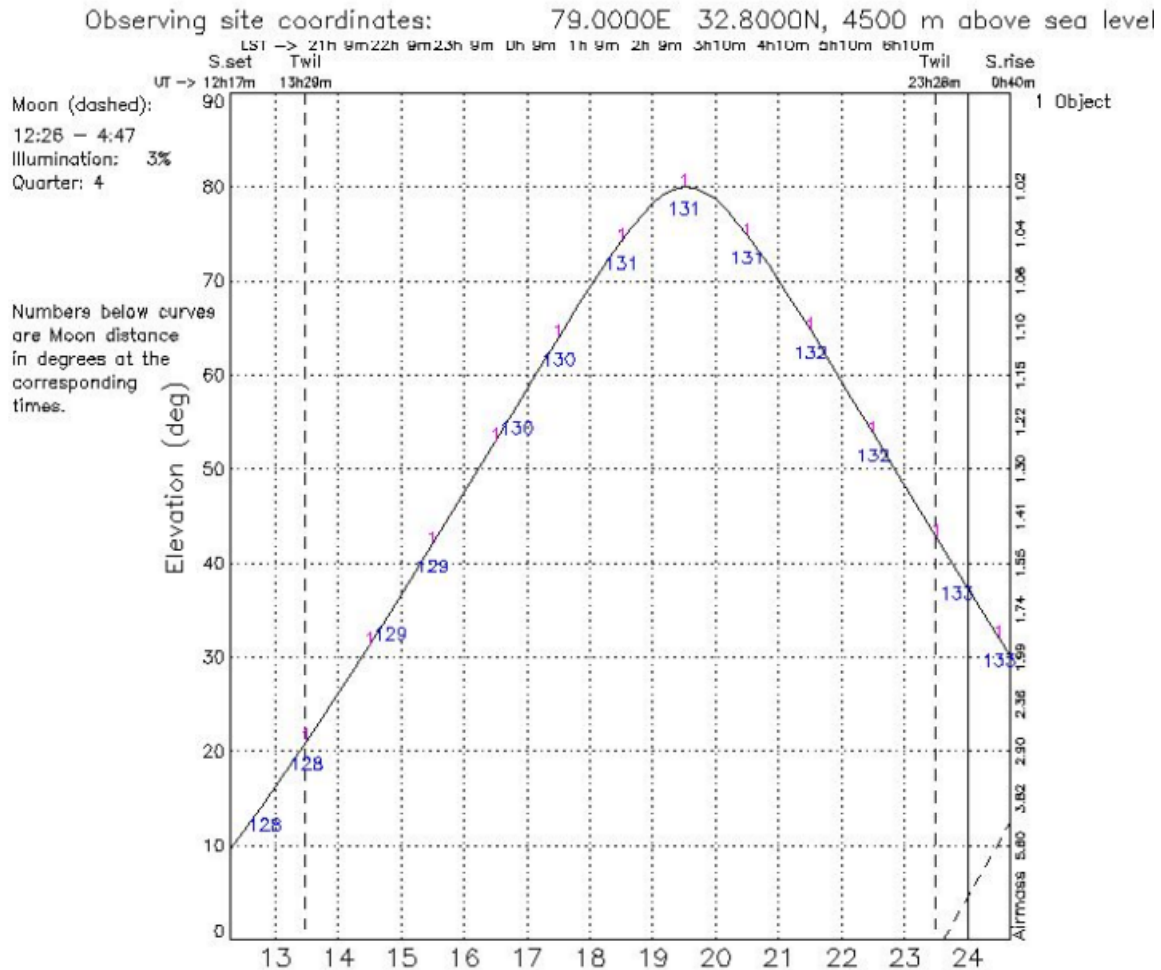


Figure 4.2: Target altitude across night and separation from the moon.

Data was acquired at uniformly spaced altitudes, corresponding to airmass values ranging from approximately 30° to 76° . For each photometric filter, a total of six science exposures were recorded, resulting in 30 light frames across all five bands. This sampling provided smooth coverage of the required airmass range for modelling the extinction behaviour.

All raw science images were first processed through a dedicated Python-based **reduction pipeline**. The pipeline first applied standard reduction, which included the corrections of master bias and master flat frames. After this, **Aperture photometry** was then performed on 20 selected stars within the field. The radii of the circular apertures for each filter were determined manually using the GUI version of APT, ensuring accurate placement based on the stellar FWHM and prevailing seeing conditions. Stars were chosen to avoid crowded regions and to ensure that their peak flux values remained well below the saturation level, thus preventing non-linear effects or flux truncation. For each star, the instrumental magnitude was computed by taking the log of the measured flux.

4.3 Results

For each photometric band, extinction coefficients were computed by performing magnitude–airmass fits for 20 stars (A–T). The final extinction coefficient for each band was obtained using a statistically weighted mean of the individual stellar coefficients, where each weight was inversely proportional to the variance of the fit. The combined extinction coefficient \bar{k}_λ and its uncertainty $\sigma_{\bar{k}_\lambda}$ were therefore calculated as

$$\bar{k}_\lambda = \frac{\sum_{i=1}^N \frac{k_{\lambda,i}}{\sigma_i^2}}{\sum_{i=1}^N \frac{1}{\sigma_i^2}}, \quad \sigma_{\bar{k}_\lambda} = \left(\sum_{i=1}^N \frac{1}{\sigma_i^2} \right)^{-1/2},$$

where $k_{\lambda,i}$ and σ_i denote the extinction coefficient and fitting uncertainty obtained from the linear regression for each star. This approach ensures that stars with more reliable fits (smaller variance) contribute more strongly to the final extinction estimate in each band.

Table 4.1: First-order atmospheric extinction coefficients by band.

Band	k_λ (extinction coeff.)	Uncertainty	Observations
<i>u</i>	0.615	0.030	Strong UV extinction
<i>g</i>	0.295	0.026	Blue scattering
<i>r</i>	0.250	0.027	Moderate
<i>i</i>	0.225	0.028	Near-IR
<i>z</i>	0.203	0.030	Minimal extinction

The relatively modest coefficient of determination ($R^2 = 0.82$) as per figure 4.5 indicates a higher degree of scatter in the data compared to shorter-wavelength bands. A likely reason for this increased scatter at longer wavelengths is that atmospheric extinction becomes progressively weaker toward the near-infrared. Because the extinction signal is smaller, the relationship between instrumental magnitude and airmass becomes less steep and therefore more sensitive to instrumental noise and sky background variations. In contrast, bands such as *u* or *g* exhibit stronger extinction, yielding tighter correlations and larger R^2 values.

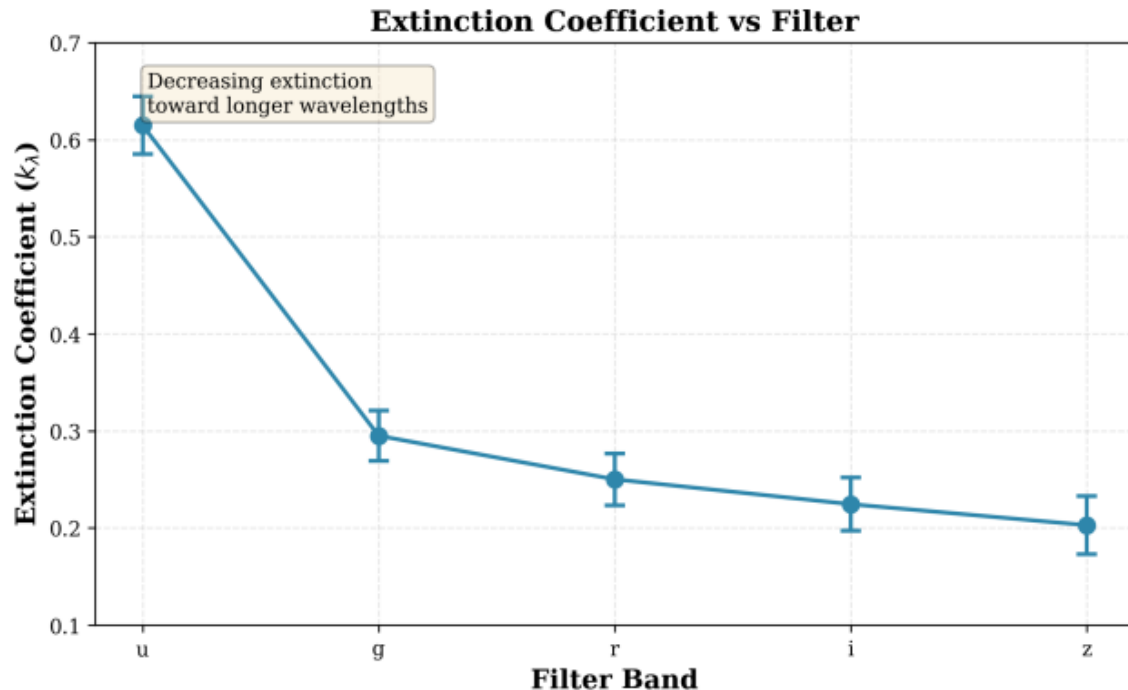


Figure 4.3: The atmospheric extinction coefficient varies across filter bands, becoming smaller at longer wavelengths since Rayleigh scattering reduces at longer wavelength.

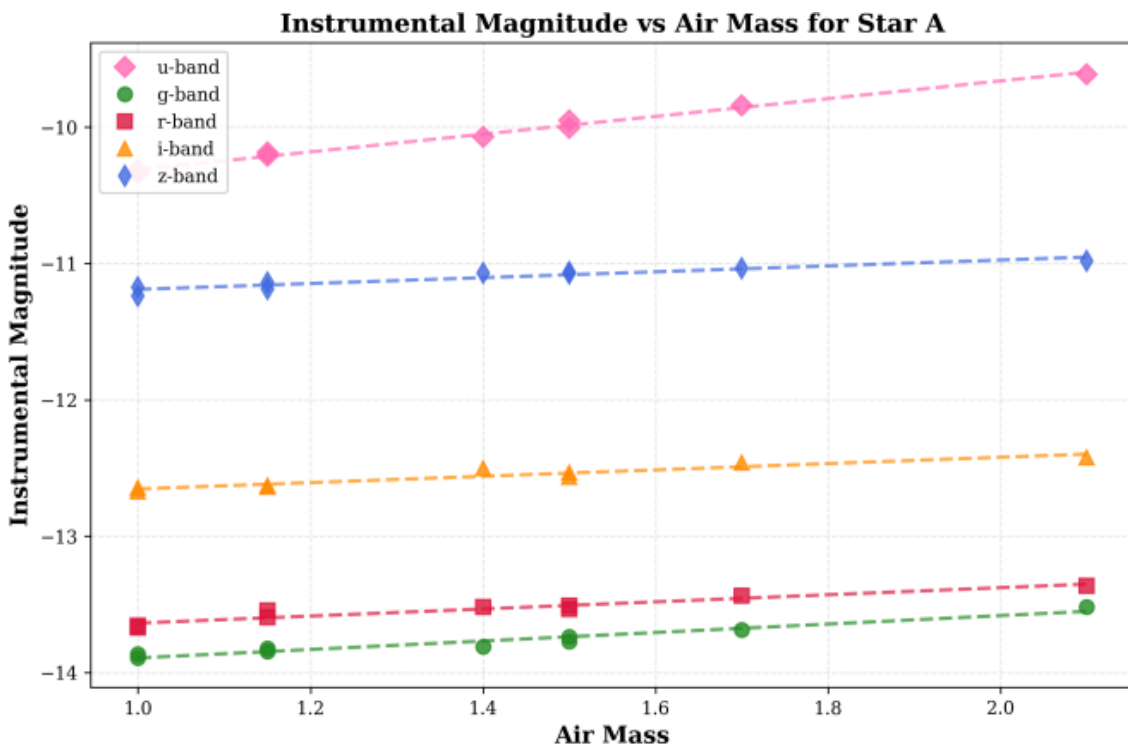


Figure 4.4: Instrumental magnitudes measured across multiple filter bands for a selected star show a clear linear relationship with airmass, where the slope in each band reflects the corresponding extinction coefficient. The best-fit trend for each filter is indicated by dashed regression lines in the plot.

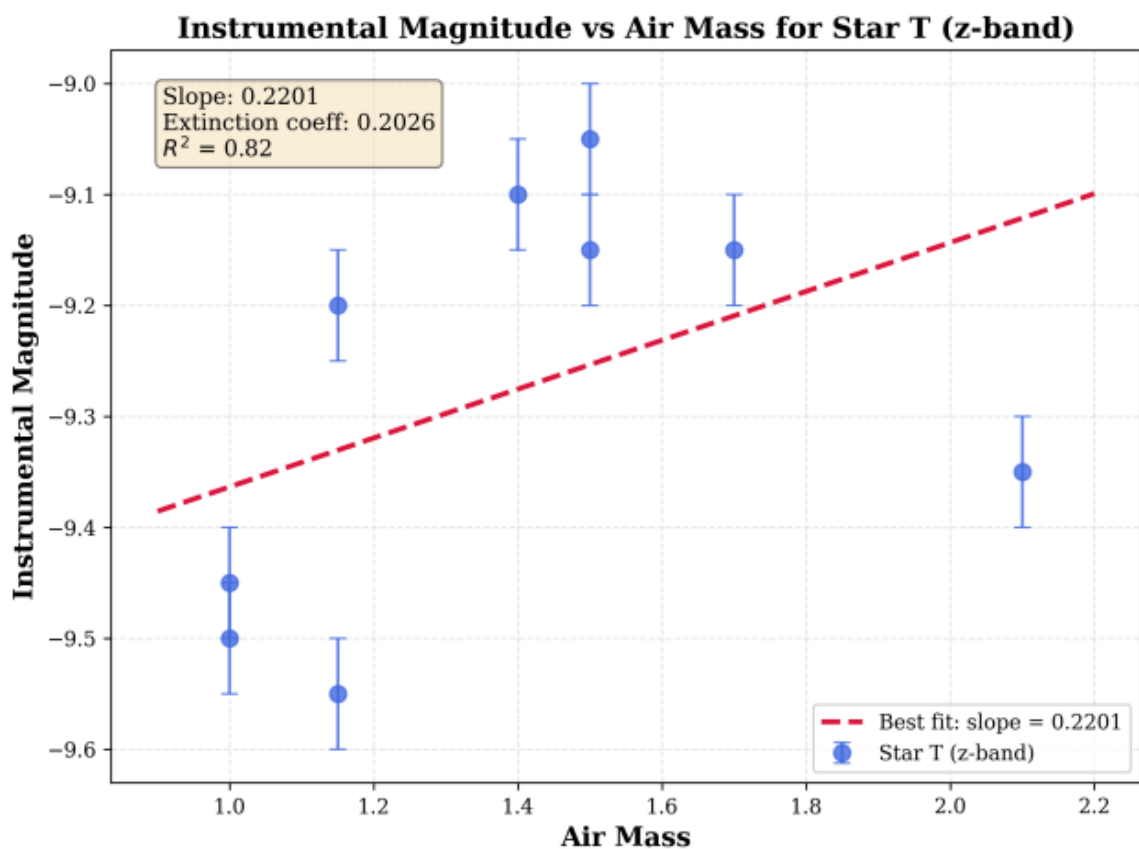


Figure 4.5: Instrumental magnitude vs. airmass for Star T in z-band. We observe a clear linear extinction trend. The slope of 0.22 corresponds to an extinction of $k_z = 0.203$

5 . Discussion

Sources of Error in CMOS characterization and Comparison with Datasheet Values

The CMOS parameters measured in this project inevitably differ from the ideal specifications quoted in the sensor datasheet (SBIG), primarily due to the combined effects of intrinsic sensor noise. Figure 5.1 illustrates the photon-transfer curve (PTC), which highlights the distinct noise regimes present in CMOS sensors. At low signal levels, read noise and fixed-pattern structure dominate, while at intermediate levels the behaviour transitions toward the Poisson regime. Small deviations from ideal slopes directly influence the precision of the gain and read-noise estimates obtained from mean-variance fitting.

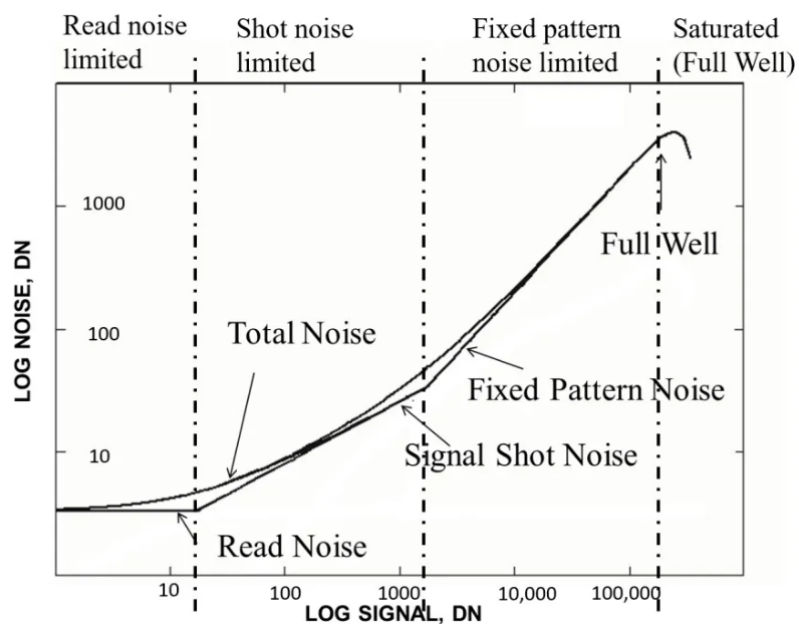


Figure 5.1: Representative photon-transfer curve showing read noise, shot noise, and fixed-pattern noise regimes. Crisp (2020)

A major source of uncertainty arises from spatial non-uniformity in flat-field images. Although a central region of interest was selected to reduce the effects

of vignetting and dust shadows, residual illumination gradients and pixel-to-pixel sensitivity variations introduce additional scatter in the variance–mean relation. These effects are amplified by temperature sensitivity: dark current doubles approximately every 5–8°C, and even minor fluctuations around the cooling setpoint can affect the measured slope of the dark-current fit.

Furthermore, real-world telescope conditions differ from the controlled laboratory environment assumed in datasheet measurements. Laboratory values are obtained under perfectly uniform illumination, stable power supply, long thermal stabilization times, and minimal electronic interference. In contrast, the observational setup used here involves twilight, telescope optics that introduce additional gradients, and ambient temperature drift, all of which contribute to deviations from ideal behavior.

Sources of Error in atmospheric extinction and Comparison with previous studies of hanle skies

The extinction coefficients derived in this work follow the expected trend of decreasing extinction from the ultraviolet to the near-infrared, reflecting the combined effects of Rayleigh scattering, aerosols, and molecular absorption. The non linear effects (as discussed in section 2.3.1) become more pronounced at higher airmass, where the increased atmospheric path length makes stellar fluxes more sensitive to thin clouds, aerosol fluctuations, and airglow variability.

To place our results in context, we compare them with the long-term study of Hanle skies by Stalin et al. (2008). Their extinction coefficients, reproduced in Fig. 5.2, were obtained from nearly year-long observations and represent a stable, averaged characterisation of the site. They report a monotonic decrease from $k_U \approx 0.36$ to $k_I \approx 0.05$.

Filter	λ_0 [Å]	k_{Ray}	k_{aer}	k_{oz}	k_{sum}
U	3650	0.3307	0.0099	0.0008	0.3414
B	4400	0.1522	0.0085	0.0005	0.1612
V	5500	0.0610	0.0071	0.0262	0.0943
R	7000	0.0229	0.0059	0.0036	0.0324
I	8800	0.0091	0.0049	0.0000	0.0140

Figure 5.2: Calculated and measured extinction coefficients for Hanle from Stalin et al. (2008)

Our coefficients follow the same wavelength dependent trend which confirms that the atmospheric behavior during our observations agrees well with the established characteristics of the Hanle site.

6 . Conclusion

This project provided a characterization of the CMOS detector used in the GROWTH-India Telescope and a measurement of atmospheric extinction across the SDSS *ugriz* bands. Through the acquisition of standard calibration frames, the detector gain, read noise, and dark current were quantified using both the mean-variance and Monitors method.

Atmospheric extinction was derived from the observations of the open cluster NGC 1039, using aperture photometry of 20 well isolated stars and Bouguer fits to determine extinction coefficients in each filter. The values exhibit the expected decrease in extinction with increasing wavelength, from the *u* band to the *z* band, and align well with trends reported in earlier characterizations of the Hanle site.

In summary, this work successfully characterized the CMOS detector performance and measured atmospheric extinction across the SDSS *ugriz* bands using calibrated observations of NGC 1039. The derived extinction coefficients follow the expected wavelength dependence and broadly agree with long term studies of the Hanle site. The overall consistency confirms the reliability of both the detector calibration and extinction analysis.

Bibliography

- 2022, AAVSO Guide to CCD/CMOS Photometry with Monochrome Cameras, American Association of Variable Star Observers (AAVSO), AAVSO 185 Alewife Brook Parkway, Suite 410 Cambridge, MA 02138. https://www.aavso.org/sites/default/files/publications_files/ccd_photometry_guide/CCDPhotometryGuide.pdf
- Crisp, R. 2020, Digital camera design, part 5: Basic noise considerations for CMOS image sensors, EDN. <https://www.edn.com/digital-camera-design-part-5-basic-noise-considerations-for-cmos-image-sensors/>
- de Astrofísica de Canarias (IAC), I. 2009, Atmospheric Extinction and Aerosol Optical Depth, url<https://www.iac.es/en/observatorios-de-canarias/sky-quality/sky-quality-parameters/atmospheric-extinction-and-aerosol-optical-depth>. <https://www.iac.es/en/observatorios-de-canarias/sky-quality/sky-quality-parameters/atmospheric-extinction-and-aerosol-optical-depth>
- Kumar, H., Bhalerao, V., Anupama, G., et al. 2022, The Astronomical Journal, 164, 90
- Pedersen, E. M., Stubbs, C. W., Fisher-Levine, M., et al. 2025, arXiv preprint arXiv:2508.17060
- Riley, A., Monroe, T., & Lockwood, S. 2016, Space Telescope STIS Instrument Science Report, 1
- (SBIG), D. L. 2022, SBIG STC-428-OEM Scientific CMOS Imaging Camera: Evaluation Package and Sensor Specifications, Diffraction Limited. <https://diffractionlimited.com/wp-content/uploads/2020/01/SBIG-STC-428-OEM.pdf>
- Stalin, C., Hegde, M., Sahu, D., et al. 2008, arXiv preprint arXiv:0809.1745
- Stubbs, C. W., High, F. W., George, M. R., et al. 2007, Publications of the Astronomical Society of the Pacific, 119, 1163
- Undege, C. 2009, in Proceedings of the 2009 Summer Computer Simulation Conference, 33–39